PERGAMON

International Journal of Solids and Structures 36 (1999) 789–812

INTERNATIONAL JOURNAL OF SOLIDS and STRUCTURES

The effect of the geometry and the load level on the dynamic failure of rotating disks

Guido Dhondt*, Manfred Köhl

MTU Motoren- und Turbinen-Union München GmbH, Postfach 50 06 40, D-80976 München, Germany

Received 27 November 1995; in revised form 20 October 1997

Abstract

The simplified and the higher order curved beam theory published previously (*International Journal of Solids and Structures* **30**(1), 137–149 (1993) and *International Journal of Solids and Structures* **31**(14), 1949–1965 (1994)) are applied to rotating disks with rectangular cross section subject to an instantaneous radial failure. The dependence of the angular size of the debris on the inner to outer radius ratio and on the load level is examined and compared with semi-empirical and experimental results in the literature. Finite element calculations confirm the results obtained with the higher order beam theory for moderate to high inner to outer radius ratios. It is shown that agreement with the experimental results can be further improved by a proper choice of the boundary conditions.

Keywords: Beam; Crack; Disk; Dynamic; Failure; Finite element; Fragmentation; Rings; Rotating

1. Introduction

In previous articles the collapse of aircraft engine disks was examined using a simplified one-dimensional curved beam theory (Köhl and Dhondt, 1993) and a higher order theory (Dhondt, 1994). The main concern was to check whether, after an instantaneous radial failure of the disk (due to a crack), a second failure would happen, and if so, at what angle φ_{cr} from the first failure. To this end, the dynamical governing equations were solved, in the simplified theory by a Laplace transformation and modal analysis, in the higher order theory by the use of finite differences. The disks at stake had an inner to outer radius ratio γ of about $\gamma = 0.25$ to $\gamma = 0.33$ which is very low, i.e. the disks were very massive. Both theories predicted a second failure at about $\varphi_{cr} = 100^\circ$ to $\varphi_{cr} = 140^\circ$ away from the first collapse, although the growth of the internal forces was slower in the higher order theory due to the overall finite wave speed. The occurrence of a second failure at about $\varphi_{cr} = 120^\circ$ from the first failure agrees with our experience and data in the literature for

* Corresponding author.

0020–7683/99/$ - see front matter
PII: S0020–7683(97)00335–1

disks similar to the aircraft disks analysed, i.e. disks for which $\gamma \leqslant 0.33$ (Suzuki and Wada, 1972). For disks with higher radius ratios γ the experimental evidence points towards smaller second failure angles φ_{cr} (Bandera et al., 1993).

Another important parameter governing φ_{cr} is the stress level ratio η defined by the ratio of the material strength (corresponding to the stress at second failure) to the nominal stress at first failure. A value $\eta > 1$ can be regarded as realistic since the disk is normally operated at design conditions which include a safety margin between the maximum design stress and the material strength. The first failure is frequently caused by external impact or by stress concentrations due to low cycle fatigue cracks while the second failure is assumed to occur when the local stress has reached the material strength.

In the present article the influence of the geometric parameter γ and the stress level ratio parameter η on the failure angle φ_{cr} is examined. After applying the simplified theory in section 2, its predictions are compared with semi-empirical theories in the literature (section 3). Next (section 4), a synopsis and critical appraisal of some test results reported in the literature is given and again a comparison with the simplified theory is made. Section 5 looks into the predictions made by the higher order theory leading to a qualitative explanation of the test results based on dispersive effects. Finally (section 6), extensive finite element calculations, when performed under the same conditions, confirm the higher order theory for $\gamma > 0.5$. However, they also show that better agreement with the experimental evidence can be obtained by carefully modelling the spatial progression of the first failure.

2. Dynamic analysis involving radial displacements only

A dynamic analysis of the rotating disk after a sudden radial failure due to unstable crack propagation involving the radial displacement as single dependent variable has been performed by Köhl and Dhondt (1993). The disk was modelled as a curved beam under centrifugal loading and the failure was assumed to occur at once over the complete cross section. The results are expressed in terms of the normalized normal force (Fig. 1)

$$N^*(\varphi, t) := \frac{N(\varphi, t)}{q_z r} = \frac{M(\varphi, t)}{q_z r^2} \tag{1}$$

where φ is the angular position ($\varphi = 0$ at the initial crack position), t is the time, N is the normal force, M is the bending moment and q_z is the centrifugal load per circumferential unit length at the center of gravity r of the cross-section. $N^*(\varphi,t)$ is plotted in Fig. 2 as a function of the angular distance φ from the initial crack position at different times after the initial failure (in Fig. 2 τ is the normalized time $\tau = t(EI/m)^{1/2}/r^2$ where E is Young's modulus, I is the moment of inertia of the cross section of the disk about an axis perpendicular to the disk plane and m is the mass per circumferential unit of length). With increasing time the values of N^* starting from $N^* \equiv 0$ at $t = 0$ increase monotonically for all φ, while every single curve exhibits a maximum value N^*_{max} over φ. The angular position φ_{max} of N^*_{max} propagates from $\varphi = 0^\circ$ to $\varphi = 180^\circ$. The functional dependence between N^*_{max} and φ_{max} is shown in Fig. 3. These quantities can be interpreted as critical values where a second failure can occur and are therefore denoted by N^*_{cr} and φ_{cr}.

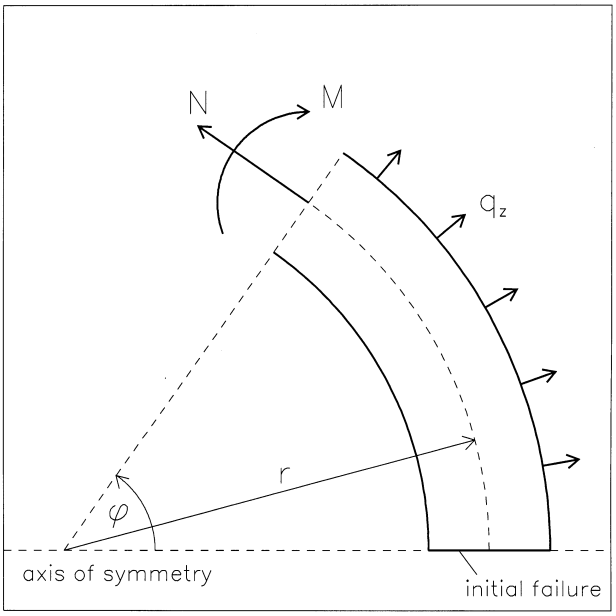

Fig. 1. Internal forces in the disk.

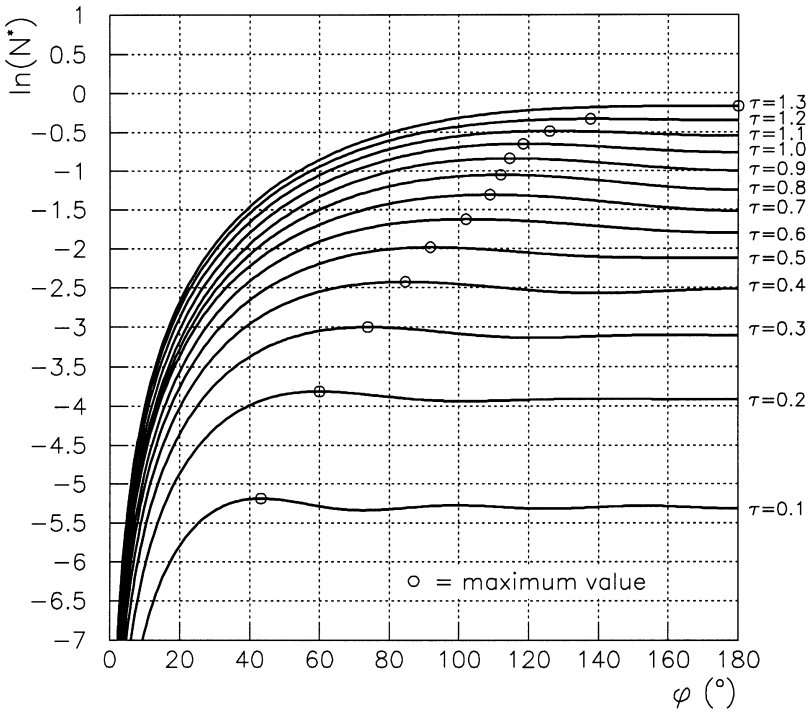

Fig. 2. Normalized normal forces at different times.

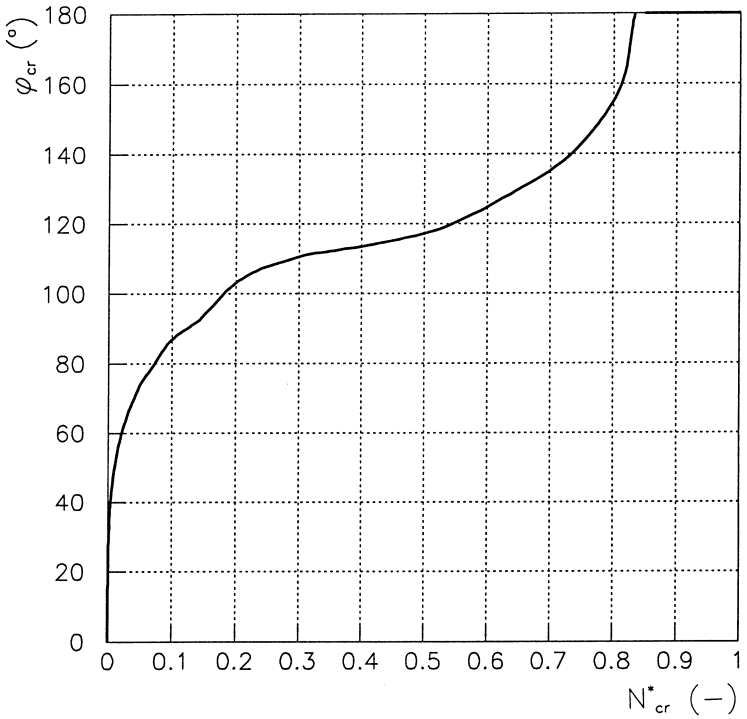

Fig. 3. Failure angle φ_{cr} as a function of the critical normalized normal force N^*_{cr}.

The circumferential stress σ_i at the inner radius r_i of the disk is dependent on the normal forces N and the bending moments M:

$$\sigma_i(\varphi, t) = \frac{N(\varphi, t)}{A} + \alpha_{ki}\frac{M(\varphi, t)}{W_i} \tag{2}$$

A is the cross section area and W_i is its moment of resistance. The coefficient α_{ki} accounts for the influence of the curvature (for a straight bar it takes the value $\alpha_{ki} = 1$), see Beitz and Küttner (1983). In the present article, only disks with rectangular cross sections are considered. After introducing the ratio γ of the inner radius r_i to the outer radius r_o, $\gamma := r_i/r_o$, the geometric quantities in eqn (2) take the form (d is the thickness of the disk)

$$A = \mathrm{d}r_o(1-\gamma)$$

$$W_i = \frac{\mathrm{d}}{r-r_i}\int_{\xi=r_i}^{r_o}(\xi-r)^2\,\mathrm{d}\xi = \frac{1}{6}\mathrm{d}r_o^2(1-\gamma)^2$$

$$\alpha_{ki} = -\frac{1}{3}\frac{1-\gamma}{1+\gamma}\left[1-\frac{1-\gamma}{\gamma\left(\frac{1+\gamma}{1-\gamma}\ln\frac{1}{\gamma}-2\right)}\right] \tag{3}$$

Substituting eqn (1) where

$$q_z = \frac{\rho\omega^2\,\mathrm{d}}{2\pi r}\int_0^{2\pi}\int_{r_i}^{r_o}\xi^2\,\mathrm{d}\varphi\,\mathrm{d}\xi = \frac{2}{3}\mathrm{d}\rho\omega^2 r_o^2\,\frac{1-\gamma^3}{1+\gamma} \tag{4}$$

(ρ is the mass density, ω is the circular frequency; this formula is more accurate than eqn (65) in Köhl and Dhondt (1993)) and eqns (3) into eqn (2) leads to

$$\sigma_i(\varphi, t) = \rho\omega^2 r_o^2 N^*(\varphi, t)\frac{1-\gamma^3}{3\gamma\left(\dfrac{1+\gamma}{1-\gamma}\ln\dfrac{1}{\gamma}-2\right)} \tag{5}$$

Let us assume that the second crack occurs at time $t = t_{cr}$ and at an angular position $\varphi = \varphi_{cr}$. Defining

$$\begin{aligned}\sigma_{i,cr} &:= \sigma_i(\varphi_{cr}, t_{cr})\\ N^*_{cr} &:= N^*(\varphi_{cr}, t_{cr})\end{aligned} \tag{6}$$

the stress level ratio parameter η is introduced by

$$\eta := \frac{\sigma_{i,cr}}{\sigma_{i,o}} \tag{7}$$

η is the ratio of the stress immediately before the second failure to the nominal stress immediately before the first failure (in an axisymmetric disk). Since $\sigma_{i,cr}$ is assumed to be equal to the material strength, η denotes the margin between the pre-failure stress and the material strength. The circumferential stress $\sigma_{i,o}$ in an uncracked disk at the inner radius is equal to (Timoshenko and Goodier, 1970)

$$\sigma_{i,o} = \rho\omega^2 r_o^2\,\frac{3+\nu}{4}\left(1+\frac{1-\nu}{3+\nu}\gamma^2\right) \tag{8}$$

(ν is Poisson's ratio). Combining eqns (5), (6), (7) and (8) we obtain the critical normalized normal force N^*_{cr} as a function of η, γ and ν:

$$N^*_{cr} = \eta\frac{3\gamma(3+\nu)\left(1+\dfrac{1-\nu}{3+\nu}\gamma^2\right)\left(\dfrac{1+\gamma}{1-\gamma}\ln\dfrac{1}{\gamma}-2\right)}{4(1-\gamma^3)} \tag{9}$$

A plot of N^*_{cr}/η as a function of γ is given in Fig. 4 (for $\nu = 0.3$).

Finally, the combination of the curves in Fig. 3 and Fig. 4 leads to Fig. 5, where the angle φ_{cr} is shown for η-values between 1.0 and 3.5 as a function of γ. It shows that φ_{cr} decreases with increasing γ and decreasing η. The dependence on η is not very outspoken. Roughly speaking (e.g. for $\eta = 1.5$), φ_{cr} attains 110° at γ about 0.33, 100° at $\gamma \approx 0.5$ and 60° at $\gamma \approx 0.9$.

Although the results were computed for the whole range $0 \leqslant \gamma \leqslant 1$, it should be noted that the theory assumes that during deformation radial cross sections remain plane, which cannot be guaranteed for small γ-values. Therefore, the results for $\gamma < 0.2$ should be handled with care.

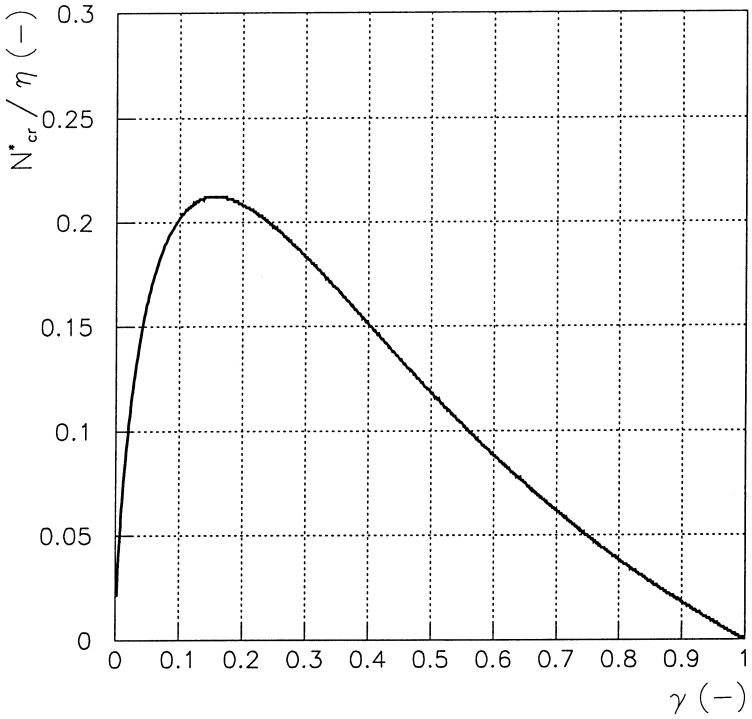

Fig. 4. Critical normalized normal force N^*_{cr} as a function of the geometric parameter γ.

3. Comparison with semi-empirical methods from the literature

In this section the semi-empirical methods derived by Bandera et al. (1993) and Langbein (1976) are discussed.

Bandera et al. (1993) start from the quasi-static forces in a disk after a first failure. These can be derived from the dynamic solution (Köhl and Dhondt, 1993) by taking the steady state limit

$$N^*_{st}(\varphi) := \lim_{t\to\infty} N^*(\varphi, t) = 1-\cos\varphi \tag{10}$$

Next, they consider the ratio of the quasi-static stress

$$\sigma_{i,st}(\varphi) := \lim_{t\to\infty} \sigma_i(\varphi, t) \tag{11}$$

(eqn (5) and eqn (10)) to the stress $\sigma_{i,o}$ immediately before the first failure (eqn (8)):

$$\frac{\sigma_{i,st}(\varphi)}{\sigma_{i,o}} = (1-\cos\varphi)\frac{4(1-\gamma^3)}{3\gamma(3+\nu)\left(1+\dfrac{1-\nu}{3+\nu}\gamma^2\right)\left(\dfrac{1+\gamma}{1-\gamma}\ln\dfrac{1}{\gamma}-2\right)} \tag{12}$$

and evaluate this ratio using experimentally determined angles $\varphi = \varphi_{cr,exp}$ at which the second failure occurred. This led to the observation that

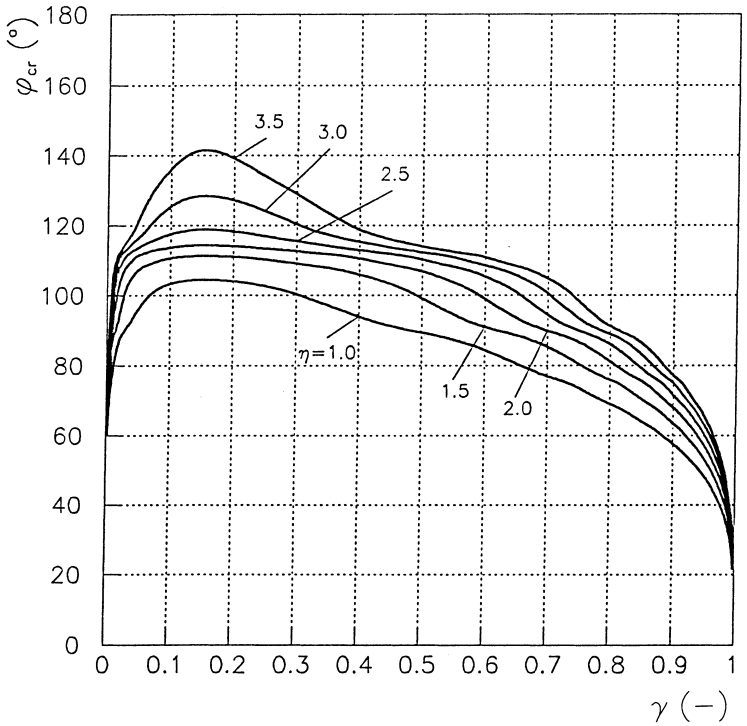

Fig. 5. Failure angle φ_{cr} according to the simplified theory.

$$\frac{\sigma_{i,st}(\varphi_{cr,exp})}{\sigma_{i,o}} \approx 7\eta \tag{13}$$

approximately holds, independently of the values of γ and v.

Bandera et al. interpret the expression 7η in eqn (13) as "dynamic stress correction factor". Indeed, the second failure is expected to occur at an angular position φ_{cr}, where the material strength ($=\eta\sigma_{i,o}$) is reached by $\sigma_{i,st}(\varphi)$. However, the angle obtained by substituting $\sigma_{i,st}(\varphi) = \eta\sigma_{i,o}$ into the quasi-static approach (eqn (12)) is much smaller than the experimental evidence. It is concluded that this discrepancy is due to the non-dynamic treatment of the problem. Therefore, according to eqn (13), the pre-crack stress level $\sigma_{i,o}$ has to be multiplied by the factor 7η in order to obtain the value of $\sigma_{i,st}(\varphi_{cr})$ leading to the right failure angle φ_{cr} when using the quasi-static approach of eqn (12). This results in the formula

$$\varphi_{cr} = \cos^{-1}\left[1 - 7\eta \frac{3\gamma(3+v)\left(1+\frac{1-v}{3+v}\gamma^2\right)\left(\frac{1+\gamma}{1-\gamma}\ln\frac{1}{\gamma} - 2\right)}{4(1-\gamma^3)}\right] \tag{14}$$

for the failure angle φ_{cr} which is shown in Fig. 6 for $\eta = 1.0$, 2.0 and 3.0 as a function of γ ($v = 0.3$). From the previous discussion it follows that the curve for $\eta = 1$ really is a model based interpolation between experimental data points, whereas the curves for $\eta > 1$ are genuine predictions.

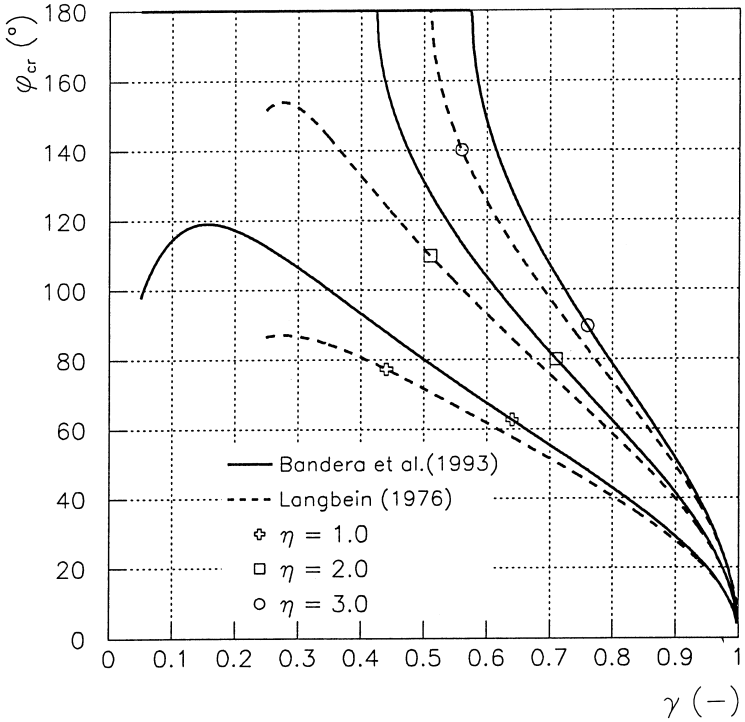

Fig. 6. Failure angle φ_{cr} according to the literature.

The experimentally determined dynamic stress correction factor 7η can be compared to a similar correction factor following from the dynamic analysis of section 2. To this end N^*_{cr} is calculated from eqn (9). Subsequently, φ_{cr} is determined from Fig. 3 and finally inserted into eqn (12). Figure 7 compares both approaches (for $\eta = 1$ and $\nu = 0.3$): up to $\gamma = 0.5$ the analytically determined correction factor is between 6 and 8; for large γ-values, however, it increases steeply.

Langbein (1976) also developed a quasi-static semi-empirical formula for the second failure angle. However, compared to Bandera et al. (1993) his simplifications are more drastic since, for example, he considers only bending moments and no normal forces for the circumferential stresses and does not account for the curvature (cf the factor α_{ki} in eqn (2)). The critical angle φ_{cr} is approximated by

$$\varphi_{cr} = 2\sin^{-1}\sqrt{\eta\frac{\gamma^5 - 2.11\gamma^4 + 5.22\gamma^3 - 8.56\gamma^2 + 4.89\gamma - 0.44}{2.78(\gamma - \gamma^4)}} \tag{15}$$

and is also shown in Fig. 6.

Although the tendency is the same, the Langbein results are consistently smaller than those by Bandera. For instance, for $\eta = 1$, the Langbein prediction for φ_{cr} does not exceed 90°. Comparison of Fig. 5 and 6 for $\eta = 1$ reveals that there is a reasonably good agreement between the simple curved beam theory and the Bandera curve for $\gamma \leqslant 0.5$, whereas φ_{cr} is much larger in the simplified theory for $\gamma > 0.5$. For instance, for $\gamma = 0.8$ the simplified theory predicts $\varphi_{cr} = 70°$, whereas

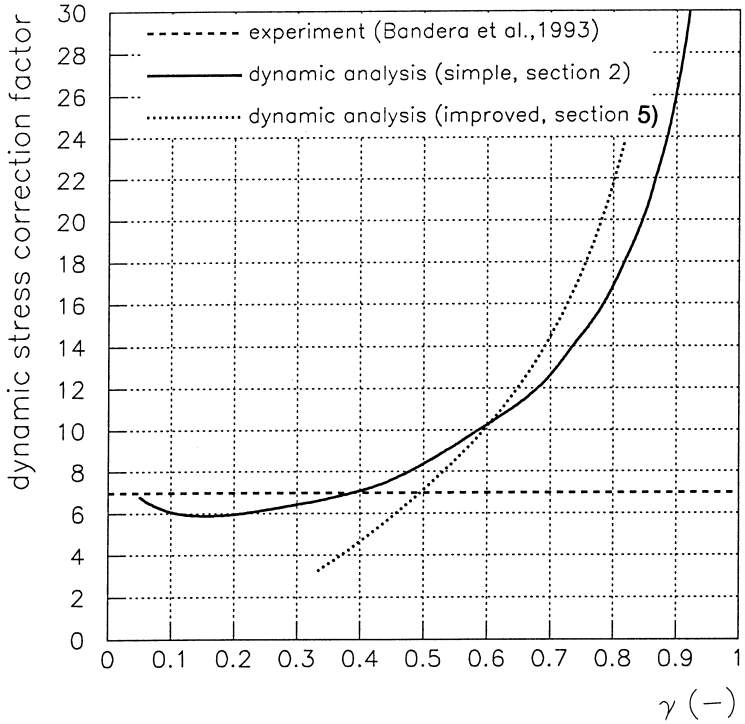

Fig. 7. Dynamic stress correction factor.

Bandera yields $\varphi_{cr} = 40^{\circ}$. Furthermore, looking at the variation of η, the simple beam results are more narrow banded than the Bandera predictions.

4. Critical appraisal of available experimental evidence

In the literature a number of very interesting test results have been reported and will be discussed here. However, it should be noted that the present account is not meant to be exhaustive so that additional material may exist the authors are not aware of.

The source for this section is the article by Bandera et al. (1993). The authors quote in Fig. 13 of their article test results by Langbein (1976), Robinson (1944), Genta and Pasquero (1988) and Hagg and Sankey (1974) showing the number of disk fragments after failure. These data are reproduced in Fig. 8. A critical analysis of these data indicates that the results of Genta and Pasquero as well as Hagg and Sankey have to be discarded, since the failures were induced by cuts or holes. Indeed, on page 674 Genta and Pasquero (1988) state: "La rottura dei dischi è stata facilitata da tre schiere di fori su raggi posti a 120° in modo tale da causare la separazione di tre frammenti di circa uguale massa" ("The failure of the disks was eased by three series of holes along radii at 120° in order to induce a separation in three pieces of about the same mass") and Hagg and Sankey (1974) state on page 115: "The disks were notched to separate into quarter fragments at the burst speed". The test performed by Robinson (1944) appears to be a genuine

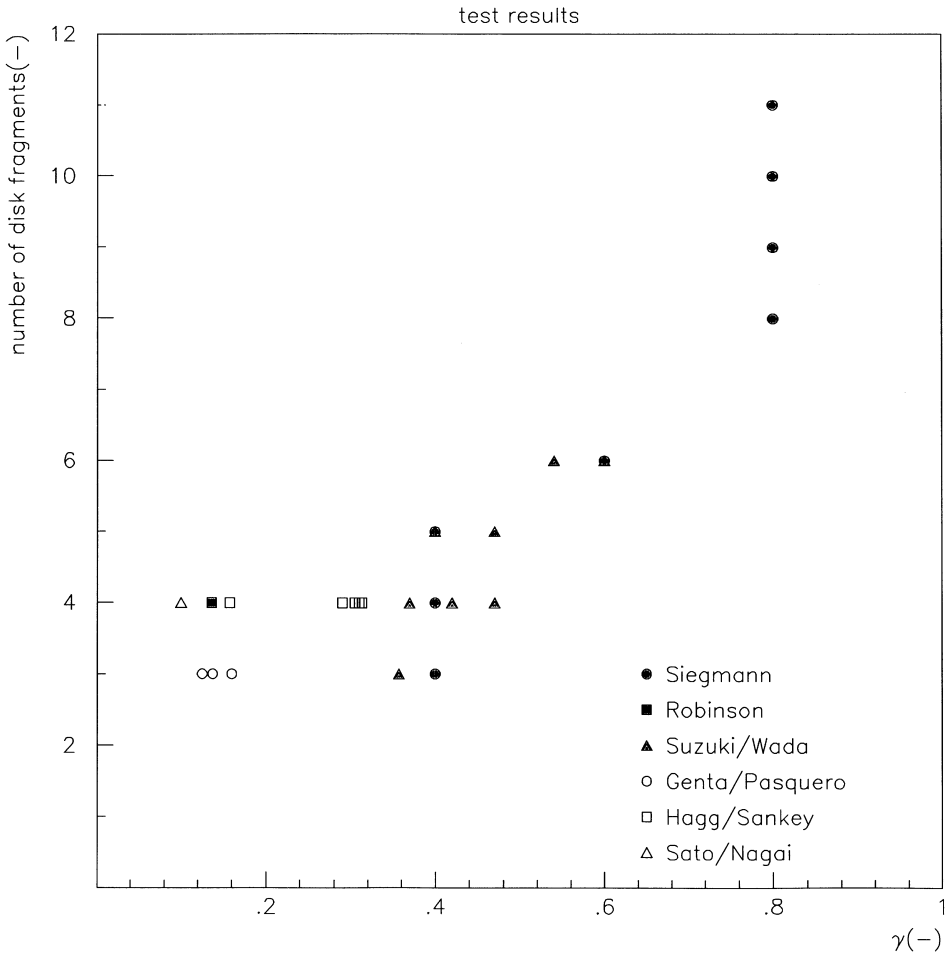

Fig. 8. Experimental results.

test on an unnotched disk at $\eta = 1$. The bulk of the test results is cited by Langbein (1976), who got them from Suzuki and Wada (1972) and Siegmann (1973). Again, the tests performed by Suzuki and Wada seem to be tests on virgin disks at $\eta = 1$. The circumstances of the very interesting results at high γ ($\gamma = 0.8$) performed by Siegmann could not be verified by the authors since the test report is unpublished. However, Siegmann (1975) reports similar test results in his Ph.D. dissertation. The tests are indeed performed at $\eta = 1$ on virgin disks. For $\gamma = 0.4$ he reports three to five debris, for $\gamma = 0.6$ five to eight debris and for $\gamma = 0.8$ ten to fifteen debris, which is even higher than the number cited by Langbein. However, looking at the only picture which is included for $\gamma = 0.8$ (Fig. 7 of the dissertation), it looks as if the size of the debris which have been counted is very dissimilar, ranging from about 45° to as small as 15°. This leads to the conclusion that the size of the debris between the first and the next failure cannot be generically determined by dividing 360° through the number of debris. Still, it is fair to say that the test results in Fig. 8 point towards a value of φ_{cr} for $\gamma \leqslant 0.4$ of about 120°, at $\gamma = 0.6$ about 60° and at $\gamma = 0.8$ about 40°.

Finally, there are a number of tests performed by Sato and Nagai (1963a, 1963b), which were cited by Bert and Paul (1995). Unfortunately, the authors did not succeed in getting a copy of these articles, and thus it is difficult to judge their validity, since the experimental setup could not be verified. The results for these tests plotted in Fig. 8 are taken from Bert and Paul (1995).

Comparing the valid test results in Fig. 8 (assuming that the disk fragments all have the same size), all represented by filled symbols, with Fig. 5, it is apparent that there is a match for $\gamma \leqslant 0.5$, whereas for $0.5 \leqslant \gamma \leqslant 1$ the curved beam predictions are too high. This phenomenon is further examined in the next sections. The Bandera et al. curve for $\eta = 1$ (Fig. 6) naturally matches the experimental data since it was derived that way. Test results for $\eta > 1$ have not been discovered. Yet, it should be emphasized that this is exactly the situation occurring in practice, where the design stress is usually distinctly smaller than the material strength. In such a case a typical cause for the first failure is a low cycle fatigue crack. Finally, as has been mentioned before, it is important to note that not all disks in the tests broke in equally sized pieces. Some of the disks tested by Suzuki and Wada (1972), for instance, after cracking along $\varphi_{cr} = 120^\circ$, cracked once more in the middle of the remaining third segment opposite to the initial crack (180° away from it). Consequently, these disks broke into four unequally sized pieces, the first two of them being larger than the remaining ones.

5. Dynamic analysis involving three displacements and three rotations

In a previous publication (Dhondt, 1994) a higher order theory was used to show that aircraft engine disks usually exhibit a second radial failure at about 100° to 140° away from a first failure. In analogy to the simplified theory, a rotating disk was considered subject to a complete radial failure and subsequent failures were analysed. In the higher order theory, however, the first failure was not introduced instantaneously. Instead, the internal forces present in the rotating disk at the failure location before failure were linearly reduced to zero within a very short time interval Δt chosen such that the numerical scheme remained stable. For instance, for $\gamma = 0.33$ a time interval $\Delta t = 2.8 \cdot 10^{-6}$ s was taken, for $\gamma = 0.82$, $\Delta t = 20.0 \times 10^{-6}$ s.

The higher order theory essentially confirmed the results of the simplified theory, although the increase of the internal forces was substantially reduced due to the inclusion of the shear deformation and rotary inertia. This led to a finite upper limit for the wave speed, a phenomenon which can also be observed by comparing the Bernoulli-Euler theory with the Timoshenko theory for a straight beam.

Section 2 illustrated that for increasing γ-values the simplified theory predicts that the second failure will occur at a smaller angle from the first failure. The same tendency is observed for small η-values (Fig. 5). Using the higher order theory, calculations were performed for a disk with a rectangular cross section (height/width = 2, height = 20 mm) for γ-values of 0.33, 0.82 and some other values in between. The circumferential stress σ_{zz} at the inside of the disk, the in-plane bending moment M_y and the axial force N are shown in Figs 9 to 11 for $\gamma = 0.33$ and in Figs 12 to 14 for $\gamma = 0.82$. All quantities were normalized by division through $\sigma_{i,o}$. φ is the angle measured from the first failure location.

At this point it seems appropriate to discuss the failure criterion used to determine the location of the second failure. In all the calculations throughout the present article and in Köhl and Dhondt

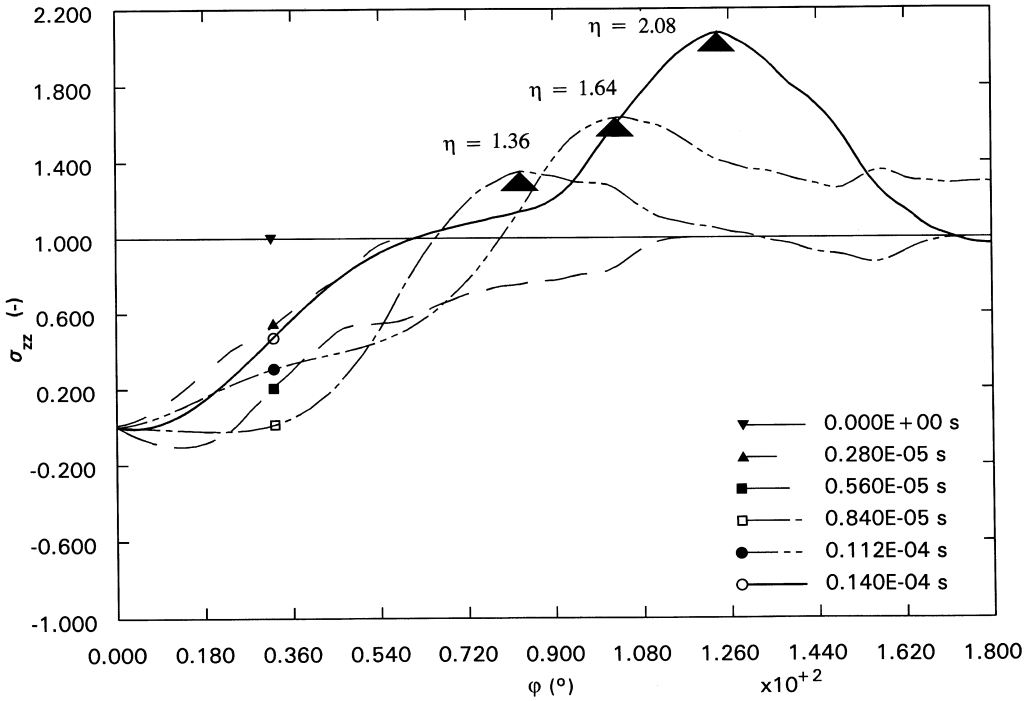

Fig. 9. Circumferential stress σ_{zz} for $\gamma = 0.33$.

(1993) as well as in Dhondt (1994) the circumferential stress at the inside of the disk was judged to be the most suitable parameter for this purpose. This corresponds to the maximum principal stress which is also generally used in crack propagation calculations (Richard, 1985; Rooke and Tweed, 1972; Yong Li Xu, 1994). The authors prefer this parameter to the von Mises stress which, in the authors' opinion, is more suitable to detect yielding rather than fracture.

In Figs 9 and 12 the maximum value along each curve is a potential second failure location and is characterized by a well-defined η-value. Indeed, if a second failure occurs at one of these maxima, it means that the corresponding stress value has reached the material strength and its normalized value (by division through $\sigma_{i,o}$) is by definition (section 1) equal to η. It is observed that, for a given value of $\eta > 1$, a second failure of $\gamma = 0.82$ (Fig. 12) will occur at a smaller angle than for $\gamma = 0.33$ (Fig. 9). For $\gamma = 0.33$ the angle also decreases for a smaller η ratio. For $\gamma = 0.82$ this tendency is reversed. Indeed, the second failure angle increases for smaller values of η. This latter phenomenon was not predicted by the simplified theory.

The circumferential stress basically consists of a contribution from the bending moment M_y and a contribution from the axial force N. Before the first failure, the bending moment and axial forces are constant along the disk ($M_y < 0$, $N > 0$), both leading to tensile circumferential stresses at the inside boundary. After the first failure, the bending moment (Figs 10 and 13) at first decreases in magnitude (and in fact drops to zero at the failure location). However, soon afterwards a minimum is created leading locally to higher tensile stresses at the inside boundary than before the failure. It is observed that this minimum propagates slower (in rad/s and m/s) for $\gamma = 0.82$ than for

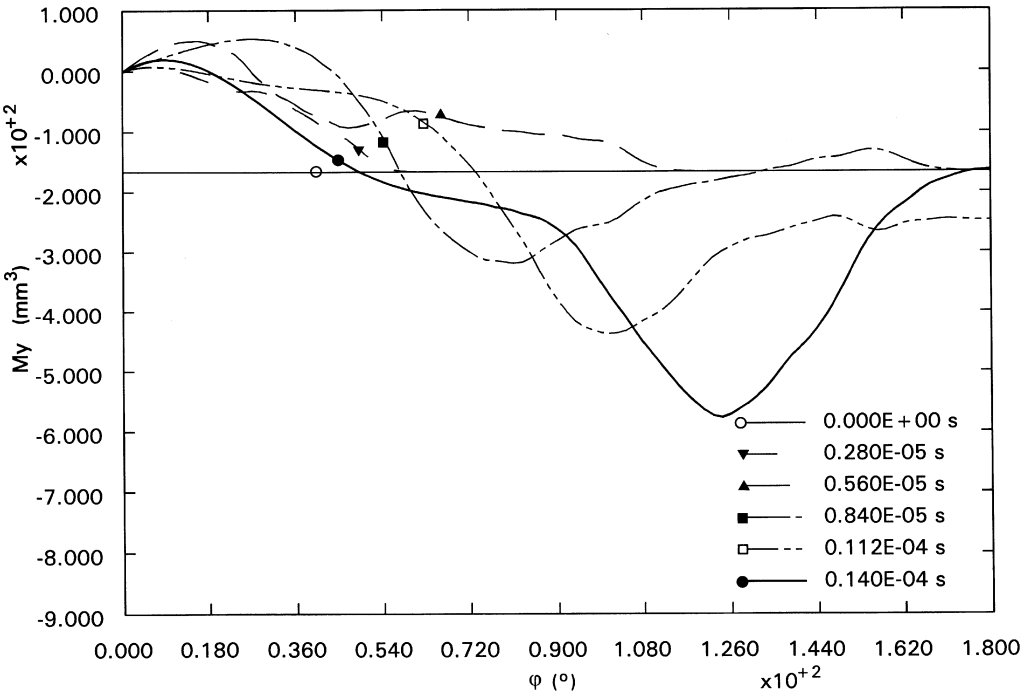

Fig. 10. In-plane bending moment M_y for $\gamma = 0.33$.

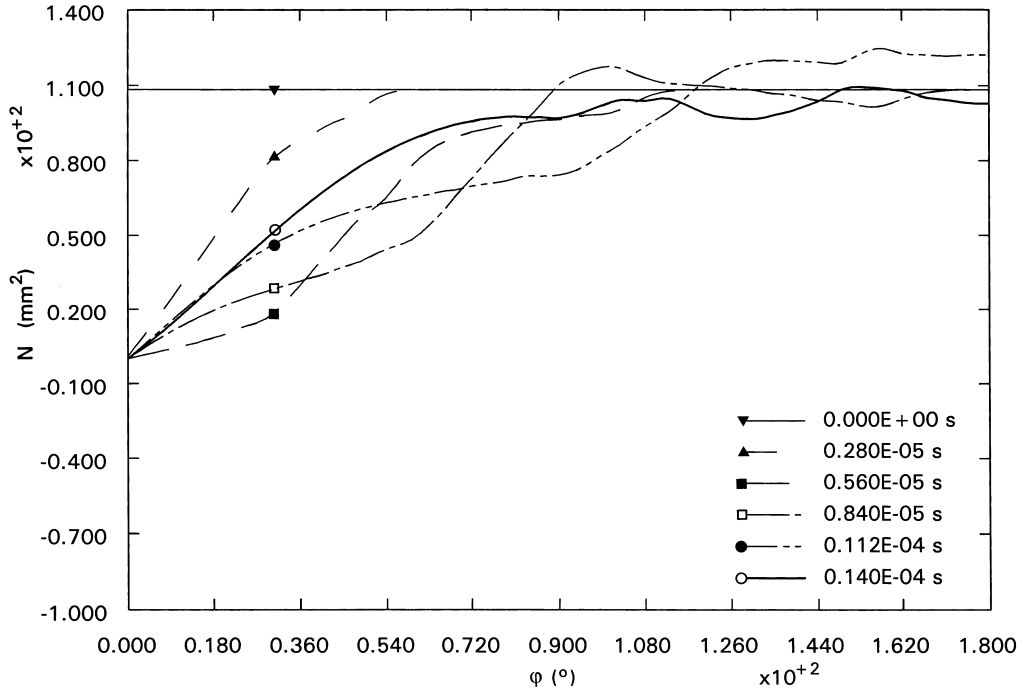

Fig. 11. Axial force N for $\gamma = 0.33$.

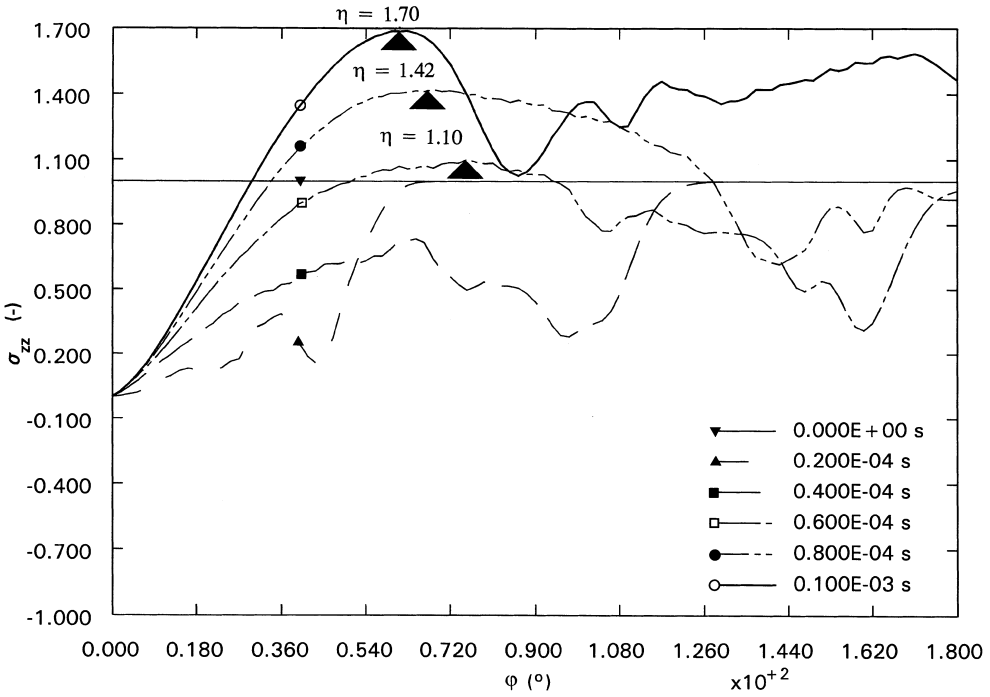

Fig. 12. Circumferential stress σ_{zz} for $\gamma = 0.82$.

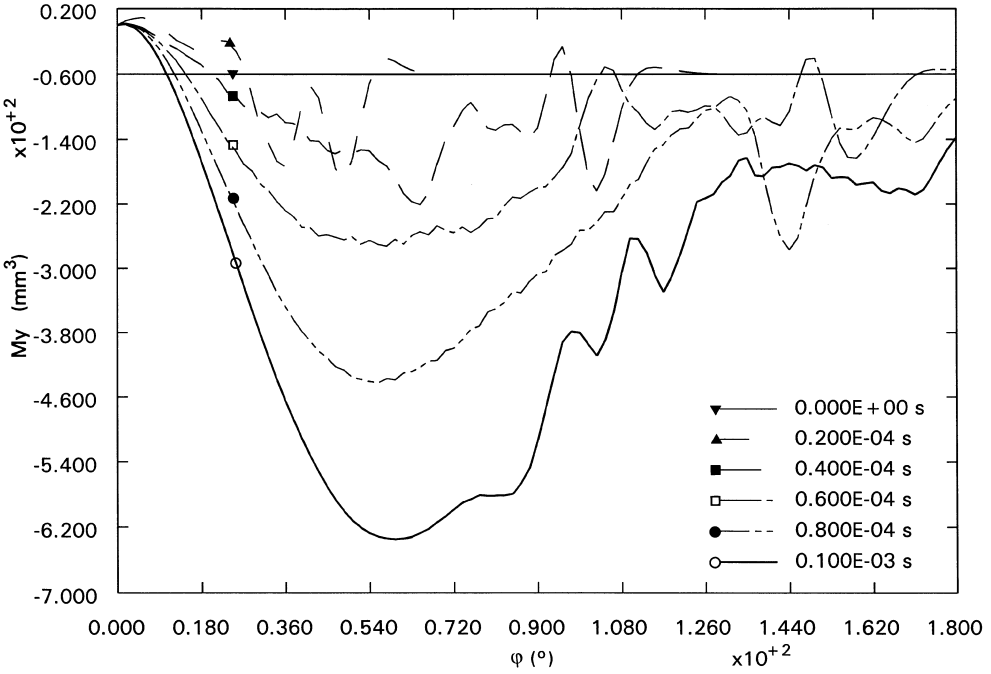

Fig. 13. In-plane bending moment M_y for $\gamma = 0.82$.

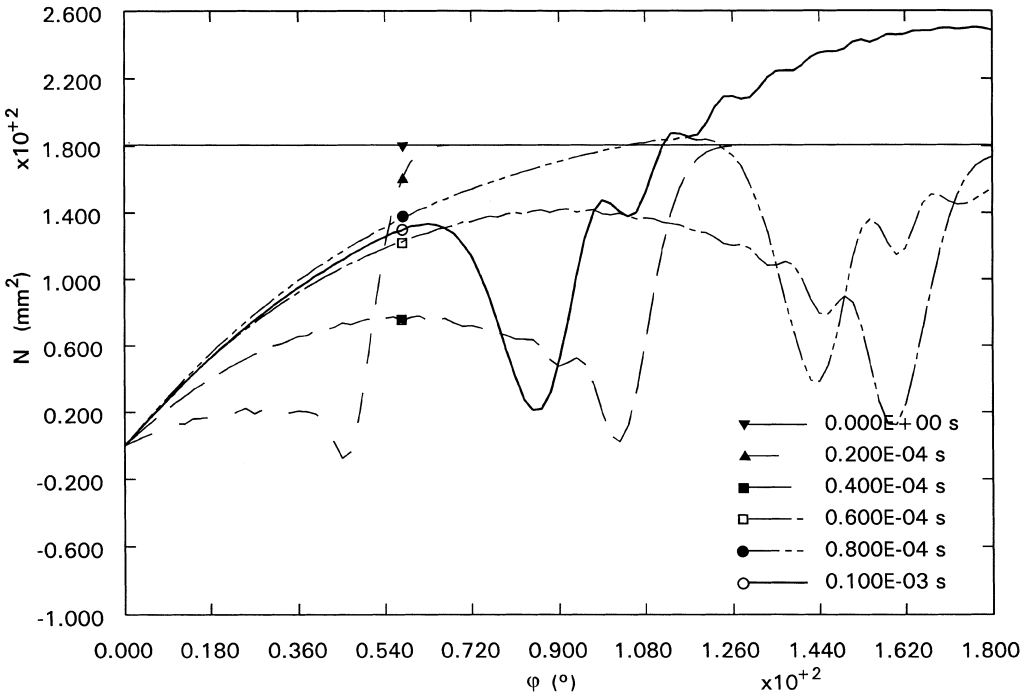

Fig. 14. Axial force N for $\gamma = 0.82$.

$\gamma = 0.33$. The axial force (Figs 11 and 14), on the other hand, basically exhibits an overall decrease after the first failure, strongest at the failure, where it is reduced to zero, less strong elsewhere. This leads to a decrease of the circumferential stress and constitutes a competing effect to the bending moment. A comparison of Fig. 14 with Fig. 11 shows that the axial force decrease preserves much more its shape for $\gamma = 0.82$ than for $\gamma = 0.33$.

The dispersion curves for $\gamma = 0.33$ and $\gamma = 0.82$ are shown in Figs 15 and 16. $\bar{\gamma}$ is the normalized wave number (normalized by division through $(I/A)^{1/2}$ where I is the moment of inertia of the cross section and A is its area) and $\bar{c}$ is the normalized wave speed (normalized by division through $(E/\rho)^{1/2}$ where E is Young's modulus and ρ is the density). The curves show that (a) the smallest axial force wave speed is higher for $\gamma = 0.82$ than for $\gamma = 0.33$; (b) the axial force and bending moment are coupled for $\gamma = 0.33$, whereas this is virtually not the case for $\gamma = 0.82$; (c) for the axial force and torque there is much more dispersion for $\gamma = 0.33$ than for $\gamma = 0.82$. Indeed, for $\gamma = 0.82$ the curves approach the straight beam curves well known from the literature (Graff, 1975).

The absence of dispersion explains the shape preservation of the axial force waves for $\gamma = 0.82$ (Fig. 14). Therefore, the sharp decrease of the axial force after the first failure keeps its shape while propagating, is reflected at $\varphi = 180^\circ$ and interacts with the slowly moving M_y-minimum yielding a circumferential stress maximum at smaller φ_{cr}-values than for $\gamma = 0.33$. It explains why the failure angle decreases for increasing γ. In the same context the reflected N-minimum leads to a decreasing φ_{cr} for increasing η, though this effect can be considered to be secondary.

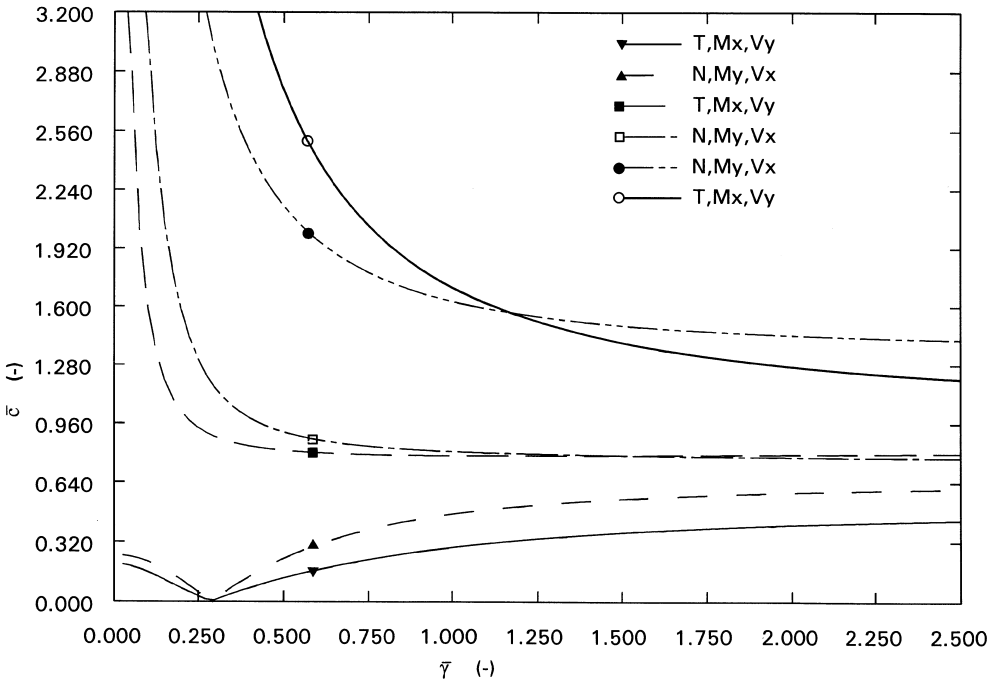

Fig. 15. Dispersion curves for $\gamma = 0.33$.

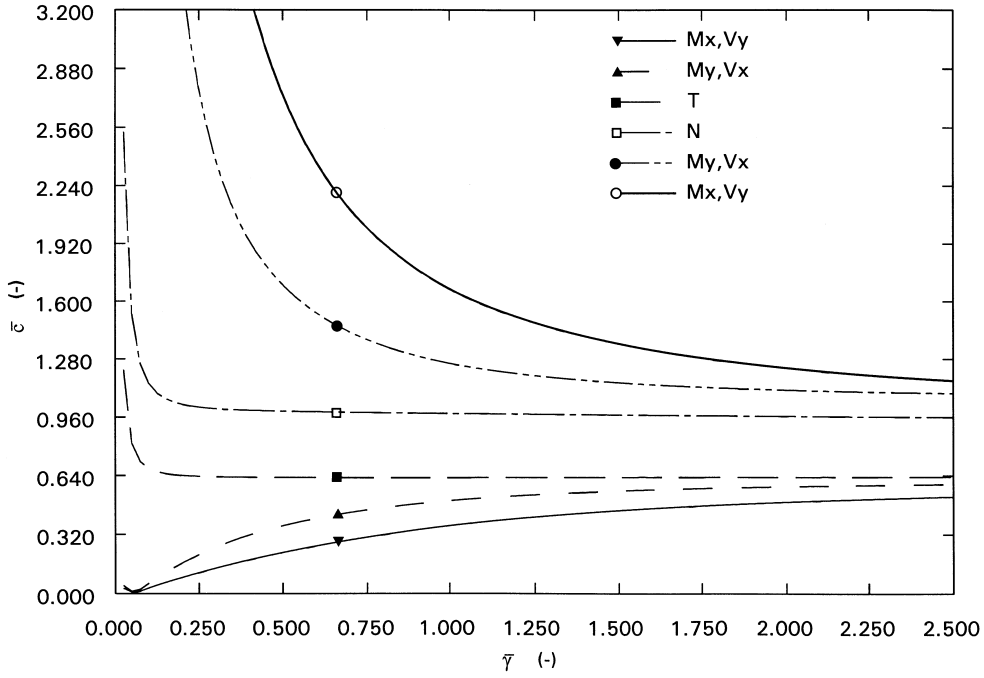

Fig. 16. Dispersion curves for $\gamma = 0.82$.

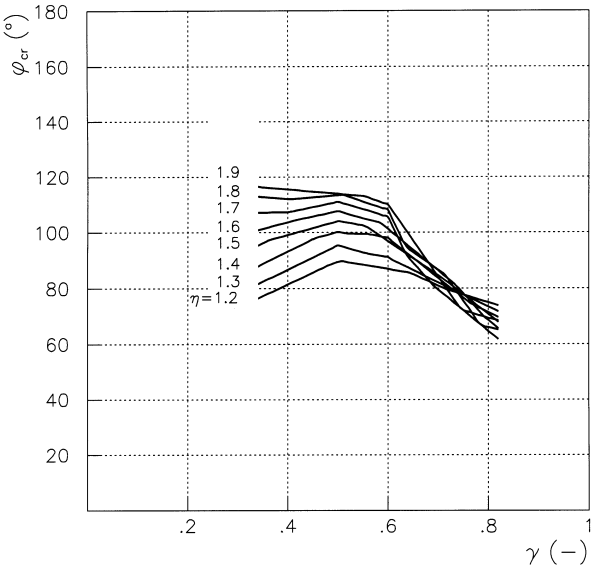

Fig. 17. Failure angle φ_{cr} according to the higher order theory vs γ (interpolation).

The maxima in Figs 9 and 12 together with results for a couple of other γ-values yield (φ_{cr}, η) tuples for discrete γ-values. Through two-dimensional interpolation *iso-*η curves were derived in a $\varphi_{cr}-\gamma$ diagram (Fig. 17). The original data points (connected by linear segments) are shown in Fig. 18. Comparing Fig. 17 with Figs 5 and 6 it is observed that apart from a relatively small area φ_{cr} consistently decreases as a function of γ. The anomalous behaviour for $\gamma < 0.45$ and $\eta < 1.8$ (see also Fig. 18) might be caused by the questionable application of a beam theory to $\gamma = 0.33$. The curves for $\eta \geqslant 1.3$ are wider apart than in the simple theory and seem to fit the Bandera et al. predictions better. However, there is still the discrepancy at $\eta \simeq 1$ and $\gamma \geqslant 0.7$, where the Bandera et al. results predict $\varphi_{cr} = 40^\circ$ and the simple and higher order theories about $\varphi_{cr} = 70^\circ$. Since this corresponds to a region where the beam theory should yield excellent results (since the disk is reduced to a slender ring), the reason for this discrepancy cannot be attributed to the theory but rather to the boundary conditions. This will be analysed in section 6. The decrease of φ_{cr} as a function of η for high γ-values, which was already noted in Fig. 12, is also very clear in Fig. 18.

6. Finite element calculations

In an effort to solve the discrepancies touched upon in the previous section, extensive finite element (FE) calculations were performed with the commerical program ABAQUS (1995) using implicit integration of the dynamic equations in the entire model. The accuracy of the calculations was checked by comparing the results obtained by two different meshes, a reasonably fine and a reasonably coarse mesh. Twenty-node three-dimensional brick elements were used throughout.

Four values of γ were analysed: $\gamma = 0.33$, $\gamma = 0.50$, $\gamma = 0.66$ and $\gamma = 0.82$. Only one half of the disk was meshed. The boundary conditions consisted of the removal of the rigid body motions

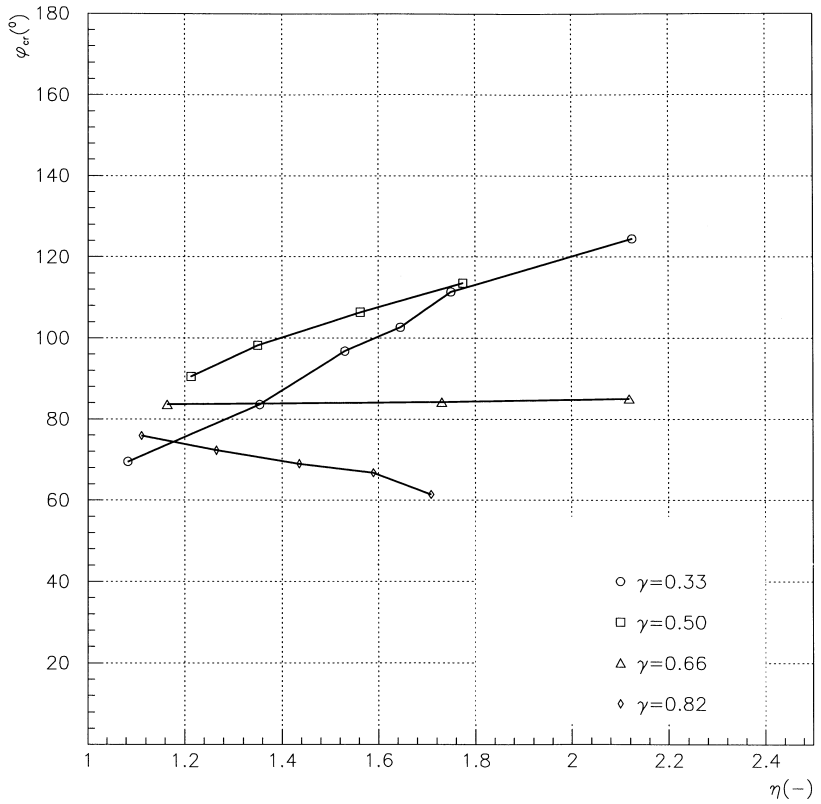

Fig. 18. Failure angle φ_{cr} according to the higher order theory vs η (data points).

and, at $t = 0$, the fixing of the symmetry plane in circumferential direction except for the crack surface (where applicable). During the calculation these latter fixings were released at the site of the first failure. The inside boundary of the disk ($\xi = r_i$) was stress-free throughout. This corresponds to a common practice in aircraft engine disks to drive the disks by means of a drive arm located somewhere between $\xi = r_i$ and $\xi = r_o$. The number of elements used in circumferential direction, over the width of the disk ($r_o - r_i$) and over the thickness d, is given in Table 1.

The calculations were genuinely three-dimensional, with $d = 10$ mm and $r_o - r_i = 20$ mm. Yet, the influence of the third dimension was not analysed, and the results are probably comparable to plane stress results. Two-dimensional calculations on disks using a quasi-static approach were recently performed by Bert and Paul (1995), yielding good agreement with the experimental evidence provided by Sato and Nagai (1963a, 1963b). However, the method and especially the boundary conditions they used were seriously questioned by the present authors (Bert and Paul, 1996; Köhl and Dhondt, 1996).

At first the higher order calculations were traced. In the same way as in the previous section the stresses at the first failure location were linearly decreased to zero within a very short time interval and uniformly over the complete cross section. The interval in the FE-calculation was chosen

Table 1
Number of elements used in the finite element calculations

γ	Mesh	Circumference	Width	Thickness
0.33	Coarse	8	4	2
	Fine	16	8	2
0.50	Coarse	10	3	2
	Fine	20	6	2
0.66	Coarse	20	3	1
	Fine	40	6	1
0.82	Coarse	32	2	1
	Fine	64	4	1

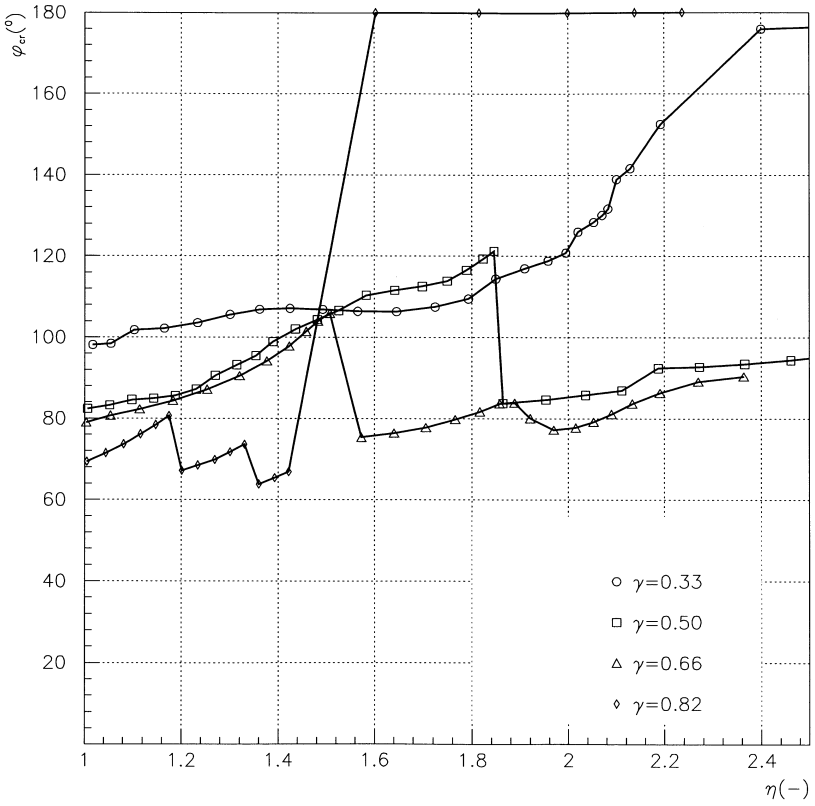

Fig. 19. Finite element results (uniform decrease of the stresses, $\Delta t \sim$ radius).

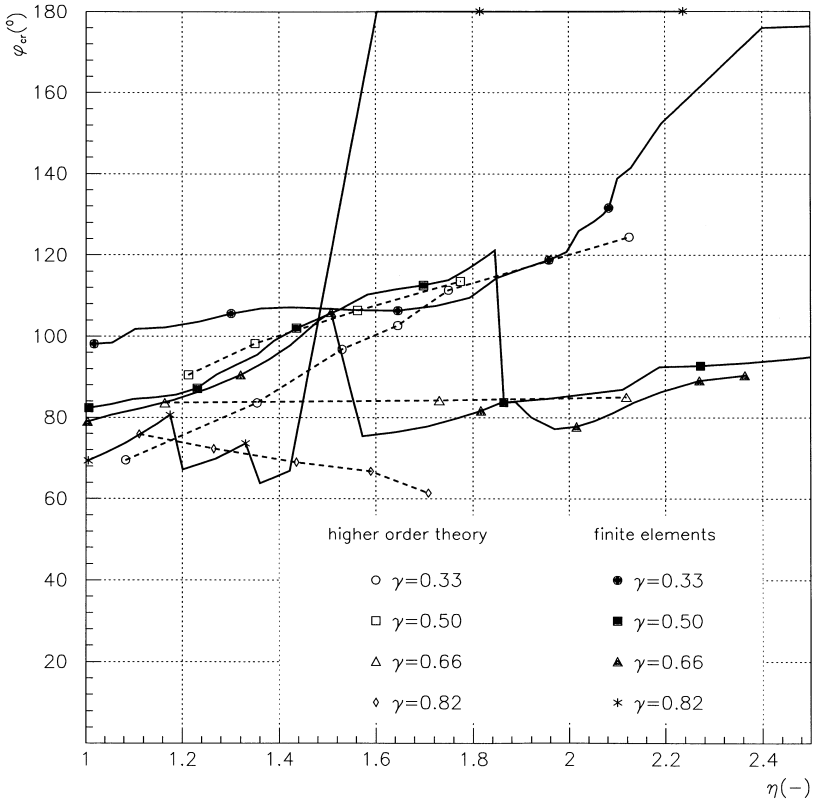

Fig. 20. Comparison between the FE calculations and higher order results.

proportional to the mean disk radius ranging from $4 \cdot 10^{-6}$ s for $\gamma = 0.33$ to 20×10^{-6} s for $\gamma = 0.82$. Though these times are not exactly identical to the ones of the higher order calculations, additional verification with exactly the same time intervals did not show any change.

The φ_{cr}–η curves are shown in Fig. 19. The strange behaviour of the higher order theory for $\gamma = 0.33$ and $\eta < 1.8$ has disappeared, indicating that the beam theory, though higher order, might not be completely appropriate in that area. The other curves (for $\gamma = 0.5$, 0.66 and 0.82) show a good qualitative agreement with the higher order theory. Figure 20 allows for a direct comparison. Although the form of the curves does not necessarily match, the general tendency is well hit. For instance, at $\gamma = 0.82$ the effect of decreasing φ_{cr} for increasing η is globally repeated, although the FE calculation points towards a stairs-like effect. At the points of discontinuity the stress maximum jumps from higher φ_{cr} values to lower ones. This same effect is observed for $\gamma = 0.5$ and $\gamma = 0.66$ at higher η-values.

Another new effect is the jump for $\gamma = 0.82$ from about 70° to 180°. This could well be linked to the geometrical nonlinearities taken into account by the FE-calculation: as the thin ring widens after the first failure, the centrifugal forces increase, leading to a distinct maximum at 180°. However, for $\gamma = 0.82$ the discrepancy with the Siegmann experiments in the form of too high values of φ_{cr} remains.

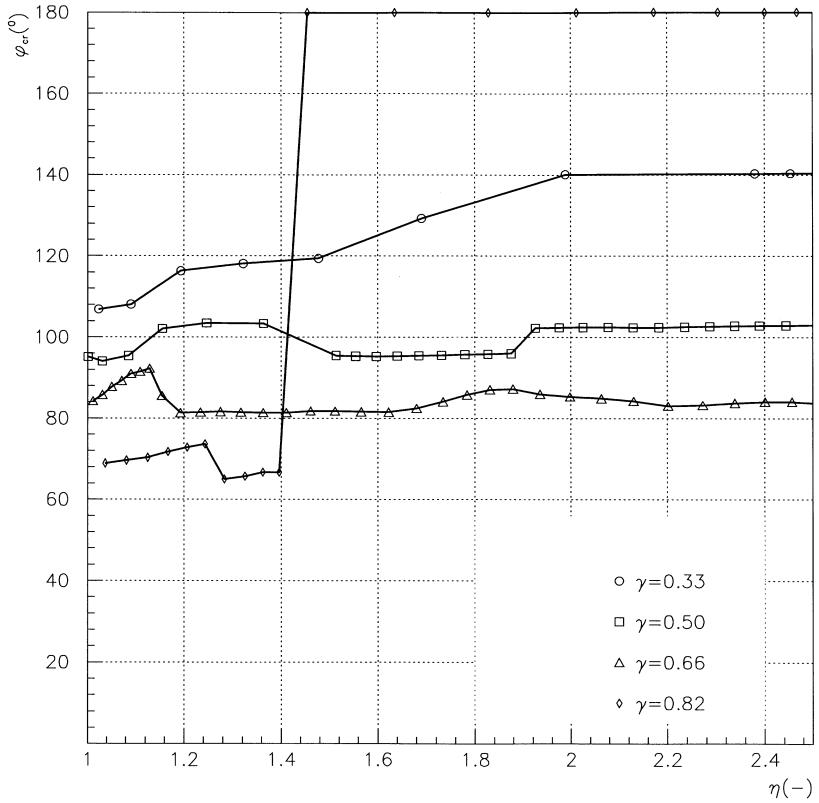

Fig. 21. FE results for $v = 600$ m/s (uniform decrease of the stresses).

In subsequent calculations Δt was varied. By looking at literature values (Machida and Yoshinari, 1986) it was acknowledged that the chosen Δt-values leading to crack propagation speeds of 1000 to 5000 m/s might be too short and that a speed of about 600 m/s for steel might be more appropriate. The way the boundary conditions at the failure location were introduced was kept the same, i.e. linearly decreasing stresses as a function of time, uniformly over the cross section. Δt was chosen to be the time needed for a crack to cross the disk width (20 mm for all disks) at a velocity of 600 m/s (Fig. 21) and 200 m/s (Fig. 22). So, contrary to the calculations leading to Fig. 19, Δt was not dependent on γ. Comparing Figs 19, 21 and 22, a gradual smoothing is observed. Qualitatively, the curves in Fig. 22 exhibit the same tendencies as in Fig. 6, except for $\gamma = 0.82$. This, again, could be related to geometrical nonlinearities.

In a further effort to improve the model for the first failure mechanism, a crack was introduced of 3.33 mm length, i.e. one sixth of the width of the disk. Starting at the crack tip, a noncontained failure propagating at a constant velocity $v = 600$ m/s was modelled by successively releasing the nodal forces along the failure cross section. In the author's opinion this is as close as one can get to the real cracking conditions and very typical for uncontained aircraft engine disk failures. The φ_{cr}–η curves are shown in Fig. 23. It is immediately noticed that for η slightly above one the results virtually coincide with the curves in Fig. 6, i.e. the Siegmann experiments are well matched.

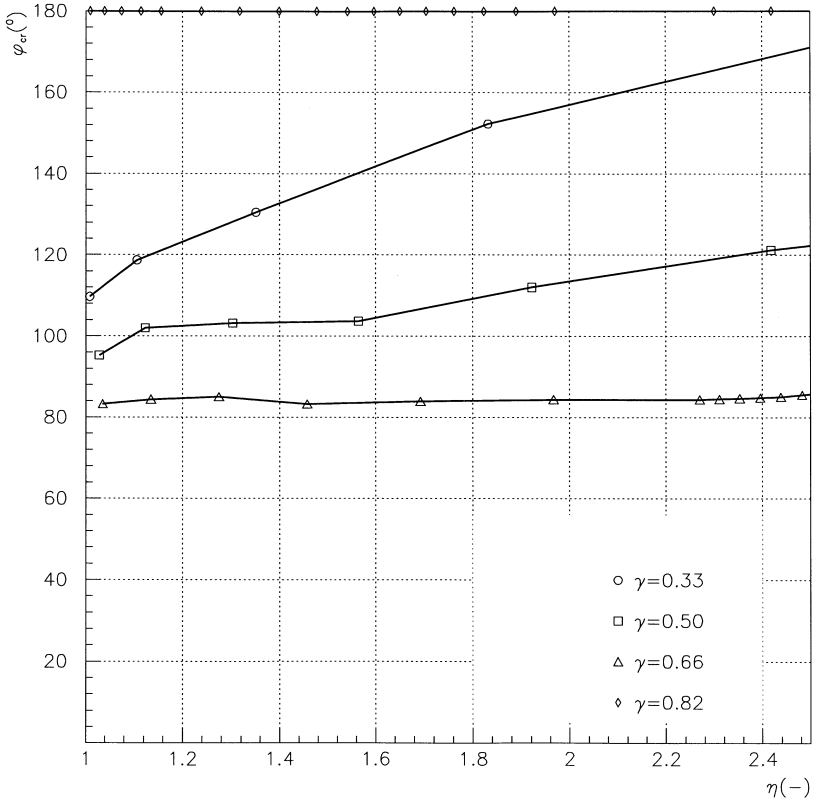

Fig. 22. FE results for $v = 200$ m/s (uniform decrease of the stresses).

Additional calculations have shown that the removal of the pre-failure crack of 3.33 mm does not change the result substantially. This seems to indicate that the accurate modelling of the radial propagation of the first failure (no matter the initial size of the crack) is of utmost importance to obtain correct results, especially for high γ-values. Though at times jumpy, there is a general tendency for φ_{cr} to increase with increasing η. This again matches the expectations quite well.

7. Conclusions

The simplified and the higher order curved beam theory published earlier for the analysis of aircraft engine disks were applied to disks with rectangular cross section for different inner to outer radius ratios γ and for different stress level ratio values η. It was shown by the simplified theory that after a first radial failure a second failure will occur at an angle φ_{cr}, which decreases for increasing γ-values and decreasing η-values. This is in qualitative agreement with semi-empirical formulas and experimental results in the literature. However, quantitatively the predictions at high γ-values and $\eta = 1$ are too high. The higher order theory basically confirmed these tendencies, but led to a modified η-dependence at high γ-values. Finite element calculations revealed that the

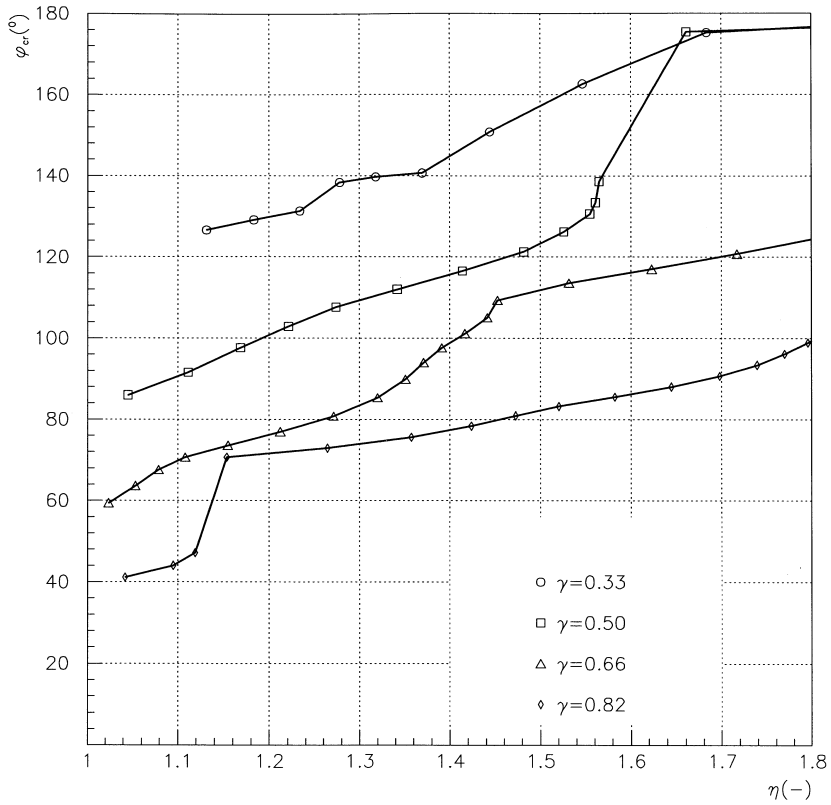

Fig. 23. FE results for an uncontained failure at a constant speed $v = 600$ m/s.

discrepancies with the test results might be attributed to the way the first failure was introduced and showed that a correct model for the spatial propagation of the first failure leads to a better agreement with the experiments.

Acknowledgements

The authors would like to thank the final reviewer for his/her detailed analysis of the paper and his/her excellent comments.

References

ABAQUS User's Manual, Version 5.5 (1995), HKS, Pawtucket, RI, U.S.A.

Bandera, C., Nicolich, M. and Strozzi, A. (1993) On the bursting mechanism in rotating rings. *J. Strain Analysis* **28,** 153–162.

Beitz, W. and Küttner, K.-H. (1983) *Dubbel*, *Taschenbuch für den Maschinenbau*, 15. Auflage. Springer, Berlin.

Bert, C. W. and Paul, T. K. (1995) Failure analysis of rotating disks. *Int. J. Solids Structures* **32,** 1307–1318.

Bert, C. W. and Paul, T. K. (1996) Authors' Closure on: Failure analysis of rotating disks. *Int. J. Solids Structures* **33,** 3645–3647.

Dhondt, G. (1994) Failure analysis of aircraft engine disks II. *Int. J. Solids Structures* **31,** 1949–1965.

Genta, G. and Pasquero, G. (1988) Prove preliminari su anelli di contenimento sollecitati dall' esplosione di rotori metallici. XVI Convegno Nazionale AIAS, L'Aquila, Italy, 667–679.

Graff, K. F. (1975) *Wave Motion in Elastic Solids*. Ohio State University Press.

Hagg, A. C. and Sankey, G. O. (1974) The containment of disk burst fragments by cylindrical shells. *J. Engng. Pwr.* **96,** 114–123.

Köhl, M. and Dhondt, G. (1993) Failure analysis of aircraft engine disks. *Int. J. Solids Structures* **30,** 137–149.

Köhl, M. and Dhondt, G. (1996) Comments on: Failure analysis of rotating disks. *Int. J. Solids Structures* **33,** 3643–3644.

Langbein, R. (1976) *Maßnahmen zur Steigerung der Sicherheit an Hochgeschwindigkeitsschleifmaschinen*. Dissertation, Rheinisch-Westfälische Technische Hochschule Aachen, Aachen.

Machida, S. and Yoshinari, H. (1986) Some recent experimental work in Japan on fast fracture and crack arrest. *Engng. Fract. Mech.* **23,** 251–264.

Richard, H.-A. (1985) Bruchvorhersagen bei überlagerter Normal- und Schubbeanspruchung von Rissen, VDI Verlag 631/85.

Robinson, E. L. (1944) Bursting of steam-turbine disk wheels. *Trans. Am. Soc. Mech. Engrs.* **66,** 373–386.

Rooke, D. P. and Tweed, J. (1972) The stress intensity factors of a radial crack in a finite rotating elastic disk. *Int. J. Eng. Sc.* **10,** 709–714.

Sato, Y. and Nagai, F. (1963a) Strength of rotating disks of brittle material like cast iron. Technical report No. NAL TR-38. National Aerospace Laboratory, Tokyo (in Japanese).

Sato, Y. and Nagai, F. (1963b) Influence of Coriolis force on the burst of rotating disk of cast iron. Technical report No. NAL TR-47. National Aerospace Laboratory, Tokyo (in Japanese).

Siegmann, E. O. (1973) *Der Einfluß des Durchmesserverhältnisses auf die Anzahl und Größe von Bruchstücken beim Fliehkraftbruch von Schleifscheiben*. Unpublished report, Technische Universität Hannover, Hannover.

Siegmann, E. O. (1975) *Das Bruchverhalten von Schleifkörperwerkstoffen bei wechselnden Belastungen*. Dissertation, Technische Universität Hannover, Hannover.

Suzuki, I. and Wada, R. (1972) Schleifscheibenbruch während der Rotation. *Werkstatt und Betrieb* **105,** 643–648.

Timoshenko, S. P. and Goodier, J. N. (1970) *Theory of Elasticity*, 3rd edn. McGraw-Hill, New York.

Yong Li Xu (1994) Stress intensity factors of a radial crack in a rotating compound disk. *Eng. Fract. Mech.* **47,** 777–791.